Journal of Materials Chemistry B

PAPER

View Article Online
View Journal | View Issue

Cite this: *J. Mater. Chem. B*, 2025, **13**, 2820

# Dual-driven biodegradable nanomotors for enhanced cellular uptake†

Jianhong Wang,[a] Andreas Polyviou,[a] Jari F. Scheerstra,[a] Shoupeng Cao,[b] Alexander D. Fusi,[a] Jingxin Shao *[a] and Jan C. M. van Hest *[a]

Received 25th November 2024,
Accepted 20th January 2025

DOI: 10.1039/d4tb02633k

rsc.li/materials-b

Hybrid nano-sized motors with navigation and self-actuation capabilities have emerged as promising nanocarriers for a wide range of delivery, sensing, and diagnostic applications due to their unique ability to achieve controllable locomotion within a complex biological environment such as tissue. However, most current nanomotors typically operate using a single driving mode, whereas propulsion induced by both external and local stimuli could be more beneficial to achieve efficient motility in a biomedical setting. In this work, we present a hybrid nanomotor by functionalizing biodegradable stomatocytes with platinum nanoparticles (Pt NPs). These Pt NPs enable two distinct propulsion mechanisms. First, near-infrared (NIR) laser irradiation causes plasmonic heating, which, due to the asymmetric shape of the stomatocytes, creates a temperature gradient around the nanomotors. Second, the catalytic properties of the Pt NPs allow them to convert hydrogen peroxide into water and oxygen, generating a chemical gradient that serves as an additional driving force. Hydrogen peroxide is thereby locally produced from endogenous glucose by a co-encapsulated enzyme, glucose oxidase. The motile features are employed to achieve enhanced accumulation within tumor cells. This nanomotor design offers a versatile approach for developing dual stimuli-responsive nanomotors that operate more effectively in complex environments.

## Introduction

Nanomotors with self-propulsion capabilities have garnered significant attention as they are able to perform diverse tasks in response to various stimuli.[1–5] They can be powered by chemical reactions, such as the conversion of locally produced hydrogen peroxide ($H_2O_2$) and reactive oxygen species (ROS), or by physical stimuli like light, ultrasound, and magnetic fields.[6–12] Among these, physically mediated propulsion methods are particularly advantageous due to their spatial control and insensitivity to the internal environment. Light-propelled nanomotors, in particular, show great promise for active drug delivery and therapeutic applications, as they can penetrate deep tissue layers and display therapeutic efficacy through the photothermal effect.[13–16] Additionally, chemical propulsion is ideal for targeting specific tissues, such as tumors or inflamed areas, where compounds like $H_2O_2$ and ROS are overproduced.[17–19] Consuming these compounds may further enhance therapeutic effects.[20,21] Most current nanomotor systems, however, lack the capability to simultaneously respond to external stimuli and internal chemical fuels – a combination that could enhance targeted motility within tissues.

In designing nanomotors for potential applications in nanomedicine, both the asymmetric placement of motile elements and the biodegradability of the vehicles are essential considerations. To meet these requirements, our group developed anisotropic bowl-shaped stomatocytes composed of biodegradable copolymers of poly(ethylene glycol)-*b*-poly (D,L-lactide) (PEG-PDLLA) building blocks.[22] These stomatocytes were further functionalized in various ways, such as by incorporating manganese dioxide particles within their cavity,[23] coating them with a hemispherical gold shell,[24] or decorating their outer surface with gold nanoparticles.[25]

Herein, we report the design of a biodegradable nanomotor that responds to both external stimuli and chemical fuels present in target tissues. This was achieved by decorating the outer surface of PEG-PDLLA stomatocytes with multifunctional platinum nanoparticles (Pt NPs) (Fig. 1). The Pt NPs, which possess both photothermal and catalytic properties, were strategically placed on the stomatocytes' outer surface, resulting in Pt-coated stomatocytes (Pt-stomatocytes) with good photothermal performance, achieving a 30% photothermal conversion

---

[a] Bio-Organic Chemistry, Departments of Biomedical Engineering and Chemical Engineering & Chemistry, Institute for Complex Molecular Systems, Eindhoven University of Technology, 5600 MB Eindhoven, The Netherlands. E-mail: J.Shao@tue.nl, J.C.M.v.Hest@tue.nl

[b] College of Polymer Science and Engineering, State Key Laboratory of Polymer Materials Engineering, Sichuan University, Chengdu 610065, P. R. China

† Electronic supplementary information (ESI) available. See DOI: https://doi.org/10.1039/d4tb02633k

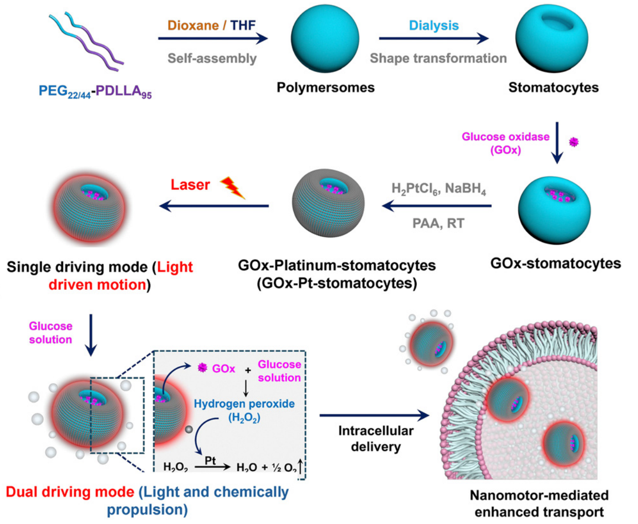

Fig. 1 Schematic illustration of the fabrication process for dual-driven biodegradable stomatocyte nanomotors, designed for efficient intracellular transport. The scheme highlights the steps involved, including the encapsulation of glucose oxidase (GOx) in the stomatocyte cavity and the decoration of platinum nanoparticles (Pt NPs) on the outer surface, enabling dual propulsion through chemical and photothermal mechanisms.

efficiency. Activation of the Pt NPs induced robust motility, reaching maximum velocities of 96 μm $s^{-1}$ due to their uneven distribution. Furthermore, the Pt-stomatocyte nanomotors demonstrated phototaxis by adjusting their movement based on the angle of irradiation. In the presence of hydrogen peroxide ($H_2O_2$), the Pt-stomatocytes exhibited autonomous motion by generating a chemical gradient that further enhanced their mobility. To ensure a continuous $H_2O_2$ supply as fuel, glucose oxidase (GOx) was encapsulated within the stomatocytes' cavity, catalyzing the conversion of glucose into gluconolactone and $H_2O_2$. Cryo-TEM analysis confirmed both the successful loading of GOx in the lumen of the stomatocytes and the deposition of Pt NPs on their outer surface. Both propulsion mechanisms – chemical and photothermal – were shown to drive the nanomotors forward. Notably, enhanced diffusion of the Pt-stomatocyte nanomotors was observed when the photothermal effect was combined with chemically-driven motion, significantly improving their accumulation capabilities in cancer cells, underscoring their potential for targeted therapy.

## Results and discussion

To construct the nanomotor framework, we synthesized two biodegradable block polymers, $PEG_{22}$-$PDLLA_{95}$ and $PEG_{44}$-$PDLLA_{95}$, through organo-catalyzed ring-opening polymerization (ROP), following previously established procedures.[22,25] Prior studies demonstrated that combining these copolymers can yield both spherical polymersomes and bowl-shaped polymersomes (stomatocytes), making them ideal candidates for the nanomotor chassis. To determine the degree of polymerization (DP) and polydispersity index (PDI), we employed proton nuclear magnetic resonance spectroscopy ($^1$H NMR) and gel permeation chromatography (GPC). As shown in Fig. S1 and Table S1 (ESI†), the block copolymers were successfully synthesized, exhibiting favorable degrees of polymerization and low polydispersity (PDI $<$ 1.1). Next, spherical polymersomes were formed *via* self-assembly of these two copolymers in a 1 : 1 weight ratio using the solvent switch methodology. Bowl-shaped stomatocytes were generated through osmotic-induced shape deformation by dialyzing the polymersome mixture against a brine solution (50 mM). Pt NPs were then prepared *in situ* and coated onto the outer surface of the stomatocytes through non-covalent interactions between the stabilizing ligand poly(acrylic acid) (PAA) of the Pt NPs and the stomatocyte surface (Fig. 2a). For comparison, spherical Pt-polymersomes were also prepared using the same method. The hydrodynamic size and morphology of the formed polymersomes, Pt-polymersomes, stomatocytes, and Pt-stomatocytes were characterized using dynamic light scattering (DLS) and cryogenic transmission electron microscopy (cryo-TEM) (Fig. 2b–f and i). The spherical morphology of the polymersomes and the curved membranes with an open neck of the stomatocytes were clearly observed. Furthermore, cryo-TEM images confirmed the successful deposition of Pt NPs on the surface of both polymersomes and stomatocytes. Additionally, the color of the stomatocytes changed from a white cloudy solution to a black solution after Pt decoration (Fig. S2, ESI†). The morphology of both polymersomes and stomatocytes was further confirmed through scanning electron microscopy (SEM), as shown in Fig. S3 (ESI†). UV-vis spectroscopy of the Pt-polymersomes and Pt-stomatocytes indicated a favorable

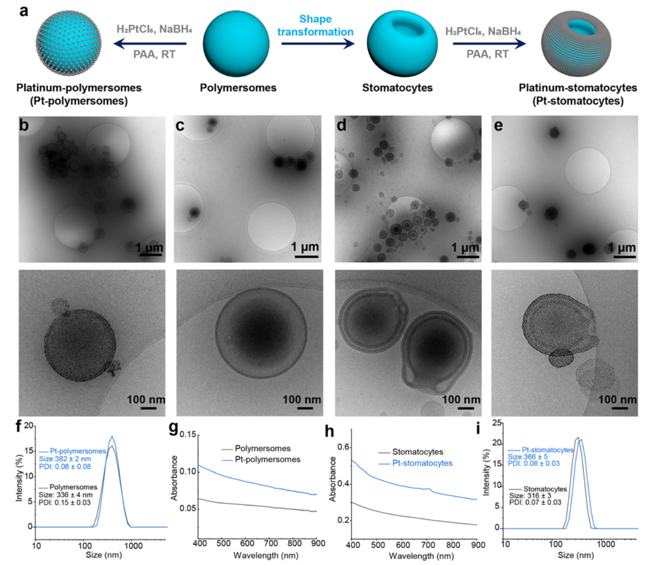

Fig. 2 Preparation and characterization of polymersomes and stomatocytes with decoration of Pt NPs on their surface. (a) Schematic illustration of the preparation of Pt NPs-modified polymersomes (Pt-polymersomes) and Pt NPs-modified stomatocytes (Pt-stomatocytes). Cryo-TEM images (zoom-out and zoom in) of (b) Pt-polymersomes; (c) polymersomes; (d) stomatocytes; and (e) Pt-stomatocytes. (f) Hydrodynamic size and (g) UV-vis spectra of polymersomes and Pt-polymersomes. (h) UV-vis spectra and (i) hydrodynamic size of stomatocytes and Pt-stomatocytes.

broad absorbance range from 650 nm to 850 nm (Fig. 2g and h), which is optimal for plasmonic heating.

Next, we evaluated the photothermal performance of Pt-stomatocytes under laser irradiation. Given their strong NIR absorption in the 650–850 nm range, we selected a commercial 808 nm laser to illuminate the nanoparticles. For comparison, we also assessed the photothermal behavior of uncoated stomatocytes and Pt-polymersomes under the same conditions. Rapid temperature increases were observed in aqueous solutions containing Pt-polymersomes and Pt-stomatocytes, demonstrating the efficient photothermal effect of the Pt nanoparticles. In contrast, the temperature changes in Milli-Q water and an aqueous solution containing the unfunctionalized stomatocytes were negligible (Fig. 3a). These findings indicate that only Pt-coated materials generate significant plasmonic heating upon laser irradiation, due to the efficient conversion of absorbed energy by Pt nanoparticles into thermal energy. Concentration-dependent heating curves were also evaluated, and an analysis of the temperature profiles demonstrated a strong correlation between rising temperatures and increasing nanoparticle concentration (Fig. 3b). We further investigated the heating performance of Pt-stomatocytes under varying laser output powers (0, 0.75, 1, and 1.2 W). As shown in the temperature profiles (Fig. 3c), the heating properties exhibited a strong correlation with both laser power and irradiation time, indicating that the photothermal effect is highly tunable. Additionally, the photothermal stability of Pt-stomatocytes was assessed through cyclic heating and cooling measurements. As shown in Fig. S4 (ESI†), the heating capacity remained consistent after 5 irradiation cycles, demonstrating the robust photothermal stability of Pt-stomatocytes. To determine their photothermal conversion efficiency (PCE), we analysed the previously obtained heating and cooling curves (Fig. S4, details provided in the ESI†). The PCE was calculated by examining the time constant for heat transfer for the Pt-stomatocytes (Fig. S5, ESI†) and water (Fig. S6, ESI†), following established methods from previous studies,[26–28] yielding an efficiency of 30%. Additionally, the photothermal response of the samples – Milli-Q water, stomatocytes, Pt-polymersomes, and Pt-stomatocytes – under laser irradiation was visually monitored using an infrared camera, as depicted in Fig. S7 (ESI†). The structural integrity of Pt-stomatocytes was further examined by cryo-TEM after 10 min of laser irradiation at 1.2 W. As shown in Fig. S8 (ESI†), the Pt-stomatocytes retained their intact morphology post-irradiation. These findings confirm that Pt-stomatocytes exhibit both thermal adjustability and morphological stability when exposed to laser irradiation.

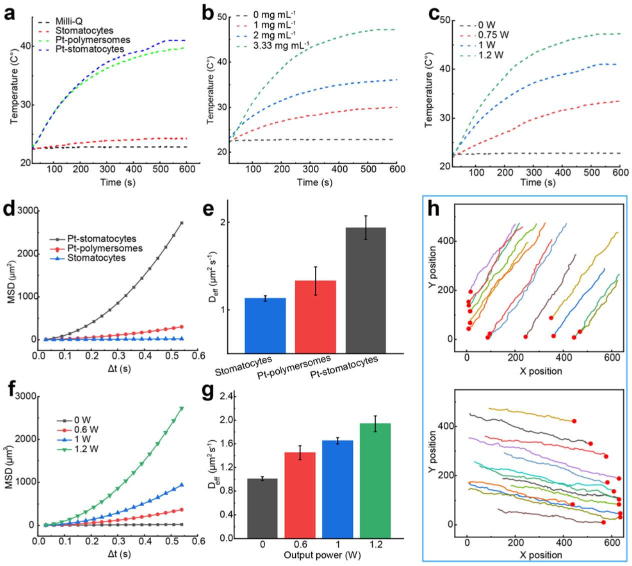

Fig. 3 Characterization of photothermal responsiveness and corresponding light-driven movement of Pt-stomatocytes. (a) Temperature profiles of irradiated aqueous media (808 nm laser irradiation, 1.2 W, 10 min) containing Milli-Q water, stomatocytes, Pt-stomatocytes, and Pt-polymersomes (all at 3.33 mg $mL^{-1}$). (b) Temperature changes of Pt-stomatocytes at varying concentrations (0, 1, 2, and 3.33 mg $mL^{-1}$) under laser irradiation (808 nm, 1.2 W, 10 min). (c) Temperature changes in an aqueous sample of Pt-stomatocytes (3.33 mg $mL^{-1}$) were analysed as a function of laser power (808 nm). (d) Mean square displacement (MSD) and (e) diffusion coefficients of Pt-stomatocytes compared to control groups (stomatocytes and Pt-polymersomes) (808 nm, 1.2 W). (f) MSDs and (g) diffusion coefficients of Pt-stomatocytes as a function of laser output power. (h) Controlled directional movement of Pt-stomatocytes under laser illumination (808 nm, 1.2 W).

To investigate the light-driven motion of our prepared nanomotors, we used nanoparticle tracking analysis (NTA) to record their movements and track their trajectories under laser irradiation. We examined the self-propulsion of Pt-stomatocytes by exposing the nanoparticles to an external 808 nm laser. From the NTA-recorded trajectories, the mean square displacement (MSD) and velocity were calculated using Golestanian's self-diffusiophoretic model.[29] Pt-stomatocytes exhibited negative phototaxis, moving directionally away from the laser source, consistent with previously reported nanomotors.[13,25] As expected, in contrast to the unfunctionalized stomatocytes control group, only Pt-stomatocytes exhibited directional motion, achieving a high velocity of 96 μm $s^{-1}$ when exposed to 1.2 W laser irradiation (Fig. 3d and e). The motion behavior of Pt-stomatocytes was furthermore highly dependent on the laser output power, as demonstrated in Fig. 3f and g and Fig. S9 (ESI†). Additionally, the directionality of Pt-stomatocytes' movement could be controlled by adjusting the laser angle (Fig. 3h).

To endow the stomatocytes with responsiveness to chemical fuel, glucose oxidase (GOx) was encapsulated into their cavities using a physical encapsulation method (Fig. 4a). Inspired by a previously reported approach,[23] we employed a physical encapsulation strategy to first load GOx into the stomatocytes, followed by the addition of genipin to crosslink GOx and prevent its release. Upon encapsulation, the solution color changed from cloudy white (stomatocytes) to light yellow (GOx-stomatocytes) (Fig. S2, ESI†). The successful encapsulation of GOx was confirmed by cryo-TEM (Fig. 4b) and the particle size was determined by DLS (Fig. S10a, ESI†). Subsequently, Pt NPs was again introduced, forming GOx-Pt-stomatocytes. Cryo-TEM imaging confirmed the well-defined structure of the resulting hybrid nanomotor (Fig. 4c). An increase in

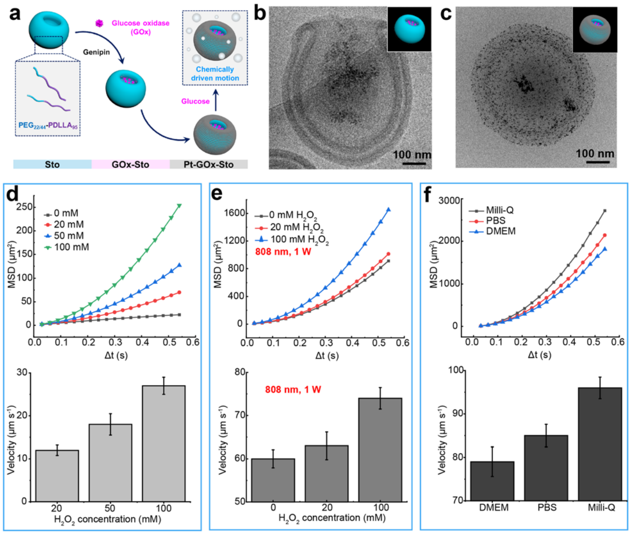

Fig. 4 (a) Schematic illustration of the GOx loading method and the chemically driven motility process. (b) Cryo-TEM analysis of GOx-loaded stomatocytes. (c) Morphological characterization of GOx-Pt-stomatocytes by cryo-TEM. (d) Mean square displacements (MSDs) and velocity of GOx-Pt-stomatocytes in the presence of varying concentrations of $H_2O_2$ (0, 20, 50, and 100 mM). (e) MSDs and velocity of GOx-Pt-stomatocytes exposed to $H_2O_2$ (0, 50, and 100 mM) under laser irradiation (808 nm, 1 W). (f) MSDs and corresponding velocity of GOx-loaded Pt-stomatocytes in different media (Milli-Q water, PBS, and DMEM) upon laser irradiation (808 nm, 1.2 W).

hydrodynamic size was observed following the coating with Pt NPs (Fig. S10b, ESI†). Additionally, the sample color changed from light yellow (GOx-stomatocytes) to black after the decoration with Pt NPs (Fig. S2, ESI†).

Next, we investigated the ability of GOx to supply $H_2O_2$ to the Pt NPs. Since glucose is more abundantly available than $H_2O_2$ under physiological conditions, the *in situ* generation of $H_2O_2$ is advantageous for ensuring a sufficient supply of chemical fuel. First, we measured the incorporation efficiency of GOx using standard colorimetric enzymatic assays (Fig. S11, ESI†). As shown in Fig. S12 (ESI†), only a small fraction ($<$10%) of the total enzyme was encapsulated within the stomatocyte cavity. However, the incorporation efficiency of GOx increased eightfold with the addition of the crosslinker genipin, confirming that genipin effectively reduced enzyme leaching.

The dual responsiveness of the Pt-stomatocytes now allowed for three modes of action; the nanomotors could be propelled *via* the addition of glucose (Fig. S13, ESI†), using NIR irradiation, or a combination of both stimuli. In this case, the asymmetric morphology of the stomatocytes was crucial for enabling motility. As anticipated, also the addition of varying concentrations of hydrogen peroxide to the Pt-stomatocytes solution produced proportional autonomous motion (Fig. 4d). In our previously reported work, we established that Au-stomatocytes had a higher density of Au nanoparticles at the bottom of their structure, as evidenced by cryo-EM and simulation results, which facilitated their motility with the neck region leading.[25] Given that Pt-stomatocytes shared a similar structure, we hypothesized that they would similarly influence the decomposition of hydrogen peroxide, with both forces driving the particles in the same direction, thereby reinforcing each other. Indeed, enhanced velocities were observed when the nanomotors were irradiated with a constant power source while exposed to varying concentrations of $H_2O_2$ (Fig. 4e). Collectively, these findings highlight the dual motion performance of our Pt-stomatocytes in response to external stimuli and chemical fuels.

To explore potential biomedical applications, we examined the motility performance of Pt-stomatocytes in phosphate-buffered solution (PBS) and Dulbecco's Modified Eagle Medium (DMEM). As shown in Fig. 4f, the Pt-stomatocyte nanomotors exhibited slightly slower motion in PBS and DMEM compared to water. This difference can be attributed to the increased viscosity of these media, consistent with prior observations.[13,14,25] Nevertheless, the variation in speed across different media remained within acceptable limits, indicating that the motile properties of the Pt-stomatocytes are preserved in a biological environment.

Encouraged by their robust motile behavior in a biomimetic environment, GOx-Pt-stomatocyte nanomotors were expected to be suitable as vehicles for the active delivery of cargo to cells. Before examining their effectiveness in intracellular delivery, we first assessed the cytotoxicity of both stomatocytes and GOx-Pt-stomatocytes toward HeLa cells using a standard CCK-8

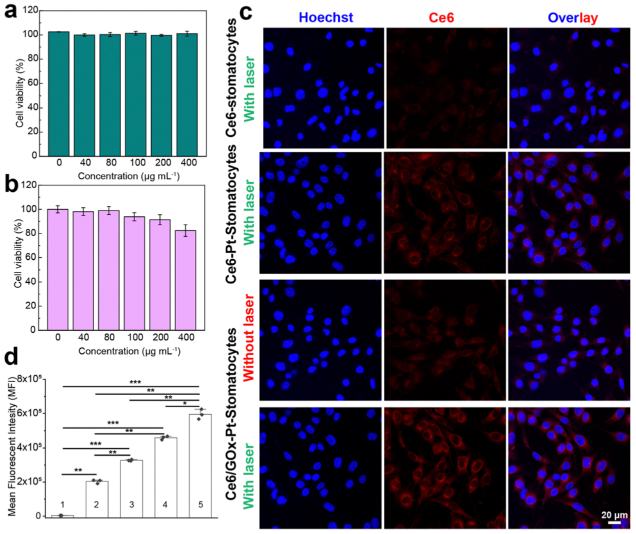

Fig. 5 Evaluation of cytotoxicity and enhanced cellular uptake of GOx-Pt-stomatocyte nanomotors. (a) Cytotoxicity induced in HeLa cells by stomatocytes and (b) GOx-Pt-stomatocytes as a function of stomatocyte concentration. (c) CLSM images of Ce6-Pt-stomatocytes (with laser irradiation, 808 nm, 1 W, 5 min) and Ce6/GOx-Pt-stomatocytes (without or with laser irradiation, 808 nm, 1 W, 5 min) after incubation with HeLa cells for 8 h. (d) The enhanced cellular uptake was evaluated by measuring the average fluorescence intensity of cells using flow cytometry. 1: PBS; 2: Ce6-Pt-stomatocyte without laser; 3: Ce6/GOx-Pt-stomatocyte without laser; 4: Ce6-Pt-stomatocyte with laser; 5: Ce6/GOx-Pt-stomatocyte with laser. All data are presented as mean ± standard deviation (SD). Statistical significance was assessed using one-way ANOVA. A significance level of 0.05 was applied, with significance denoted as follows: (*) for $p < 0.05$, (**) for $p < 0.01$, and (***) for $p < 0.001$.

assay. As shown in Fig. 5a and b, both stomatocytes and GOx-Pt-stomatocytes demonstrated high biocompatibility, with cell viability remaining above 80%. Next, we investigated the accumulation and penetration behavior of GOx-Pt-stomatocytes in HeLa cells. To track their behavior in a biological environment, fluorescent chlorin e6 (Ce6) molecules were loaded into the hydrophobic domain of the stomatocytes using previously established protocols[18,30] (Fig. S14, ESI†). Pre-cultured HeLa cells were treated with Ce6/GOx-Pt-stomatocytes under varying laser outputs (808 nm, 0 or 1 W) for 5 min. The cells were subsequently incubated and imaged by CLSM after an additional 8 h of co-culture. As a control, Ce6-stomatocytes were also introduced to HeLa cells. A notable increase in red fluorescence was observed in the Ce6/GOx-Pt-stomatocyte group, especially when exposed to external laser irradiation (Fig. 5c and Fig. S15, ESI†). The enhanced cellular uptake was further verified by flow cytometry (Fig. 5d and Fig. S16, ESI†). These results were in accordance with the CLSM observations. From these experiments we can also conclude that a dual driving force improves the accumulation of the active particles, and a higher penetration efficiency can be achieved. Finally, we investigated the therapeutic outcomes of Ce6/GOx-Pt-stomatocyte nanomotors. As shown in Fig. S17 (ESI†), the nanomotor displayed an effective therapeutic effect.

## Conclusions

In summary, we have developed a dual stimulus-driven biodegradable stomatocyte nanomotor by encapsulating glucose oxidase (GOx) in the nanocavity and decorating the outer surface with platinum nanoparticles (Pt NPs) (GOx-Pt-stomatocytes). This design leverages the plasmonic heating susceptibility and catalytic activity of Pt NPs. Under laser irradiation, the Pt-stomatocytes demonstrated strong photothermal performance, achieving a photothermal conversion efficiency of 30% due to the NIR absorption of Pt NPs at 808 nm. Laser activation enabled efficient motility, with the nanomotors reaching a velocity of 96 $\mu m\ s^{-1}$ upon exposure to a 1.2 W laser source. Additionally, GOx-Pt-stomatocyte nanomotors displayed autonomous movement in presaence of $H_2O_2$. By combining these propulsion methods, further velocity enhancement was achieved. Finally, the good motility of the GOx-Pt-stomoatocyte nanomotors was validated in a cell culture, demonstrating efficient accumulation within tumor cells.

## Author contributions

J. W., J. S.and J. C. M. H. conceived the project and designed the experiments. J. S.and J. C. M. H. supervised the research. J. W. and A. P. performed the experiments and analyzed the data. J. S. performed the flow cytometry experiments and analyzed the results. S. C. and A. F. helped to analyze the data and provided valuable advice. J. W., J. S.and J. C. M. H. co-wrote the manuscript.

## Data availability

The data presented in the documents are available upon reasonable request.

## Conflicts of interest

There are no conflicts to declare.

## Acknowledgements

This study was financially supported by The Netherlands Ministry of Education, Culture and Science (Gravitation Program 024.005.020), the Spinoza premium SPI 72-259, and the European Union's Horizon 2020 research and innovation program Marie Sklodowska-Curie Innovative Training Networks (ITN) Nanomed (No. 676137) and BIOMOLMACS (No. 859416). J. Wang thanks the support from the China Scholarship Council.

## References

1 J. Wang and W. Gao, *ACS Nano*, 2012, **6**, 5745–5751.
2 H. Wang and M. Pumera, *Chem. Rev.*, 2015, **115**, 8704–8735.
3 M. Sitti, *Nat. Rev. Mater.*, 2018, **3**, 74–75.
4 J. X. Li, B. E. F. de Avila, W. Gao, L. F. Zhang and J. Wang, *Sci. Robot*, 2017, **2**, eaam6431.
5 H. Y. Zhang, Z. S. Li, C. Y. Gao, X. J. Fan, Y. X. Pang, T. L. Li, Z. G. Wu, H. Xie and Q. He, *Sci. Robot*, 2021, **6**, eaaz9519.
6 Z. Wu, M. Zhou, X. Tang, J. Zeng, Y. Li, Y. Sun, J. Huang, L. Chen, M. Wan and C. Mao, *ACS Nano*, 2022, **16**, 3808–3820.
7 T. Li, Z. Liu, J. Hu, L. Chen, T. Chen, Q. Tang, B. Yu, B. Zhao, C. Mao and M. Wan, *Adv. Mater.*, 2022, **34**, e2206654.
8 H. Choi, J. Yi, S. H. Cho and S. K. Hahn, *Biomaterials*, 2021, **279**, 121201.
9 E. Karshalev, B. Esteban-Fernandez de Avila and J. Wang, *J. Am. Chem. Soc.*, 2018, **140**, 3810–3820.
10 D. A. Wilson, R. J. Nolte and J. C. van Hest, *J. Am. Chem. Soc.*, 2012, **134**, 9894–9897.
11 M. Wan, H. Chen, Q. Wang, Q. Niu, P. Xu, Y. Yu, T. Zhu, C. Mao and J. Shen, *Nat. Commun.*, 2019, **10**, 966.
12 J. Tong, D. Wang, Y. Liu, X. Lou, J. Jiang, B. Dong, R. Dong and M. Yang, *Proc. Natl. Acad. Sci. U. S. A.*, 2021, **118**, e2104481118.
13 J. X. Shao, S. P. Cao, D. S. Williams, L. K. E. A. Abdelmohsen and J. C. M. van Hest, *Angew. Chem., Int. Ed.*, 2020, **59**, 16918–16925.
14 S. P. Cao, J. X. Shao, H. L. Wu, S. D. Song, M. T. De Martino, I. A. B. Pijpers, H. Friedrich, L. K. E. A. Abdelmohsen, D. S. Williams and J. C. M. van Hest, *Nat. Commun.*, 2021, **12**, 2077.
15 A. Pena-Francesch, J. Giltinan and M. Sitti, *Nat. Commun.*, 2019, **10**, 3188.
16 H. Arami, S. Kananian, L. Khalifehzadeh, C. B. Patel, E. Chang, Y. Tanabe, Y. T. Zeng, S. J. Madsen, M. J. Mandella,

A. Natarajan, E. E. Peterson, R. Sinclair, A. S. Y. Poon and S. S. Gambhir, *Nat. Nanotechnol.*, 2022, **17**, 1015–1022.

17 C. Y. Gao, Y. Wang, Z. H. Ye, Z. H. Lin, X. Ma and Q. He, *Adv. Mater.*, 2021, **33**, 2000512.

18 J. H. Wang, J. J. Liu, Y. Sümbelli, J. X. Shao, X. Y. Shi and J. C. M. van Hest, *J. Controlled Release*, 2024, **372**, 59–68.

19 H. Y. Zhang, Z. Q. Zhao, S. N. Sun, S. Zhang, Y. Q. Wang, X. B. Zhang, J. Sun, Z. G. He, S. W. Zhang and C. Luo, *Nat. Commun.*, 2023, **14**, 255.

20 J. Z. Zhu, T. T. Xiao, J. L. Zhang, H. L. Che, Y. X. Shi, X. Y. Shi and J. C. M. van Hest, *ACS Nano*, 2020, **14**, 11225–11237.

21 W. P. Fan, N. Lu, P. Huang, Y. Liu, Z. Yang, S. Wang, G. C. Yu, Y. J. Liu, J. K. Hu, Q. J. He, J. L. Qu, T. F. Wang and X. Y. Chen, *Angew. Chem., Int. Ed.*, 2017, **56**, 1229–1233.

22 I. A. B. Pijpers, L. K. E. A. Abdelmohsen, D. S. Williams and J. C. M. van Hest, *ACS Macro Lett.*, 2017, **6**, 1217–1222.

23 I. A. B. Pijpers, S. P. Cao, A. Llopis-Lorente, J. Z. Zhu, S. D. Song, R. R. M. Joosten, F. H. Meng, H. Friedrich, D. S. Williams, S. Sanchez, J. C. M. van Hest and L. K. E. A. Abdelmohsen, *Nano Lett.*, 2020, **20**, 4472–4480.

24 J. X. Shao, S. P. Cao, H. L. Che, M. T. De Mertino, H. L. Wu, L. K. E. A. Abdelmohsen and J. C. M. van Hest, *J. Am. Chem. Soc.*, 2022, **144**, 11246–11252.

25 J. H. Wang, H. L. Wu, X. W. Zhu, R. Zwolsman, S. R. J. Hofstraat, Y. D. Li, Y. T. Luo, R. R. M. Joosten, H. Friedrich, S. P. Cao, L. K. E. A. Abdelmohsen, J. X. Shao and J. C. M. van Hest, *Nat. Commun.*, 2024, **15**, 4878.

26 M. H. Shi, J. L. Zhang, J. C. Li, Y. Fan, J. H. Wang, W. J. Sun, H. Yang, C. Peng, M. W. Shen and X. Y. Shi, *J. Mater. Chem. B*, 2019, **7**, 368–372.

27 Y. T. Luo, H. L. Wu, X. Zhou, J. H. Wang, S. Er, Y. D. Li, P. L. W. Welzen, R. A. J. F. Oerlemans, L. K. E. A. Abdelmohsen, J. X. Shao and J. C. M. van Hest, *J. Am. Chem. Soc.*, 2023, **145**, 20073–20080.

28 Q. L. Zou, M. Abbas, L. Y. Zhao, S. K. Li, G. Z. Shen and X. H. Yan, *J. Am. Chem. Soc.*, 2017, **139**, 1921–1927.

29 J. R. Howse, R. A. L. Jones, A. J. Ryan, T. Gough, R. Vafabakhsh and R. Golestanian, *Phys. Rev. Lett.*, 2007, **99**, 048102.

30 J. X. Shao, I. A. B. Pijpers, S. P. Cao, D. S. Williams, X. H. Yan, J. B. Li, L. K. E. A. Abdelmohsen and J. C. M. van Hest, *Adv. Sci.*, 2019, **6**, 1801678.